

In Situ Charge Modification within Prussian Blue Analogue Nanocubes by Plasma for Oxygen Evolution Catalysis

Wen-Bin Wang, Hai-Jie Cao,* and Guo-Ling Li*



Cite This: *Inorg. Chem.* 2023, 62, 10241–10248



Read Online

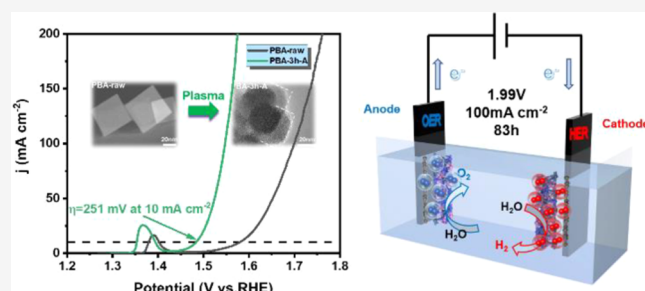
ACCESS |

Metrics & More

Article Recommendations

Supporting Information

ABSTRACT: A targeted defect-induced strategy of metal sites in a porous framework is an efficient avenue to improve the performance of a catalyst. However, achieving such an activation without destroying the ordered framework is a major challenge. Herein, a dielectric barrier discharge plasma can etch the $\text{Fe}(\text{CN})_6$ group of the NiFe Prussian blue analogue framework in situ through reactive oxygen species generated in the air. Density functional theory calculations prove that the changed local electronic structure and coordination environment of Fe sites can significantly improve oxygen evolution reaction catalytic properties. The modified NiFe Prussian blue analogue is featured for only 316 mV at a high current density (100 mA cm^{-2}), which is comparable to that of commercial alkaline catalysts. In a solar cell-driven alkaline electrolyzer, the overall electrolysis efficiency is up to 64% under real operation conditions. Over 80 h long-time continuous test under 100 mA cm^{-2} highlights superior durability. The density functional theory calculations confirm that the formation of OOH^* is the rate-determining step over Fe sites, and $\text{Fe}(\text{CN})_6$ vacancy and extra oxygen atoms can introduce charge redistribution to the catalyst surface, which finally enhances the oxygen evolution reaction catalytic properties by reducing the overpotential by 0.10 V. Both experimental and theoretical results suggest that plasma treatment strategy is useful for modifying the skeletal material nondestructively at room temperature, which opens up a broad prospect in the field of catalyst production.



1. INTRODUCTION

The pursuit of high-performance electrocatalysts for sustainable energy storage and conversion systems has been a key step to meet the growing energy demand and fossil fuel consumption.^{1–5} Oxygen evolution reaction (OER) is a crucial process for driven water cracking,^{6–8} fuel cell,⁹ and rechargeable metal–air cell.^{10,11} However, the slow dynamics of the multistep OER need high energy consumption and accordingly limit the overall energy conversion efficiency, especially in water splitting.^{12,13} Noble metal oxides (RuO_2 and IrO_2) have been proven to be effective OER catalysts, although widespread application is still limited by their high cost.^{14–17}

Prussian blue analogue (PBA) with dispersed non-noble metal sites has been reported to be a promising candidate to catalyze some specific reactions with high selectivity and efficiency.^{18–21} However, PBA itself is difficult to be used as an OER catalyst directly (due to poor conductivity and high overpotential). Anionic modulation is highly promising to improve the catalytic performance of PBA framework-based electrocatalysts, such as oxides, phosphides, and sulfides.^{22–24} However, in this case, the PBA framework is always damaged completely and the high dispersion of metal sites is largely lost, resulting in reduced catalytic activity.

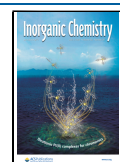
Defect-induced strategy is another effective way to achieve excellent catalytic activity, including steps, corners, dislocation, vacancy, and amorphous domains.^{25–28} The generation of

defects may change the local electronic environment, which subsequently enhances the energetics of local metal sites.²⁹ However, the stability of the framework is always dramatically affected after modification. A nondestructive modification under mild conditions is highly desirable. The previous literature has proved that hyperactive ion species generated by plasma can overcome the energy barrier to break the metal-cyano coordination bond and produce open metal sites.^{10,24,29,30} Inspired by this, we used low-temperature air plasma by dielectric barrier discharge (DBD) to etch the porous PBA framework and activate the metal sites.³¹ Benefiting from the low thermal effect and high chemical reactivity, the DBD plasma can selectively modify the PBA electrocatalysts without destroying the framework.

In this work, we synthesized a kind of defect-rich bimetallic cubic NiFe PBA, in which one-third $\text{Fe}(\text{CN})_6$ units are missing. Active oxygen species excited in the DBD air plasma can directly attach to the open metal sites or substitute the

Received: March 28, 2023

Published: June 20, 2023



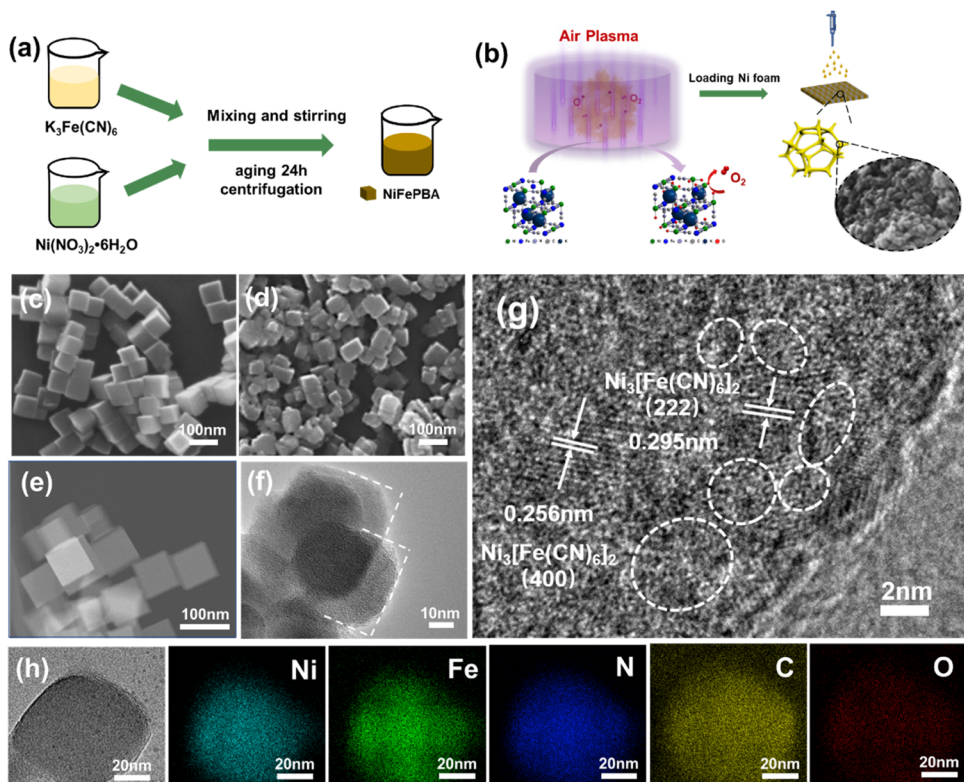


Figure 1. (a, b) Schematic diagram of the synthesis process of NiFe PBA by the DBD plasma. Scanning electron microscopy (SEM) image of the morphological characterization of (c) NiFe PBA and (d) PBA-3h-A. (e, f) HRTEM. (g) Lattice diagram of HRTEM. (h) High-angle annular dark-field scanning transmission electron microscopy (HAADF-STEM) image of PBA-3h-A and its corresponding element mapping images of Ni, Fe, C, N, and O.

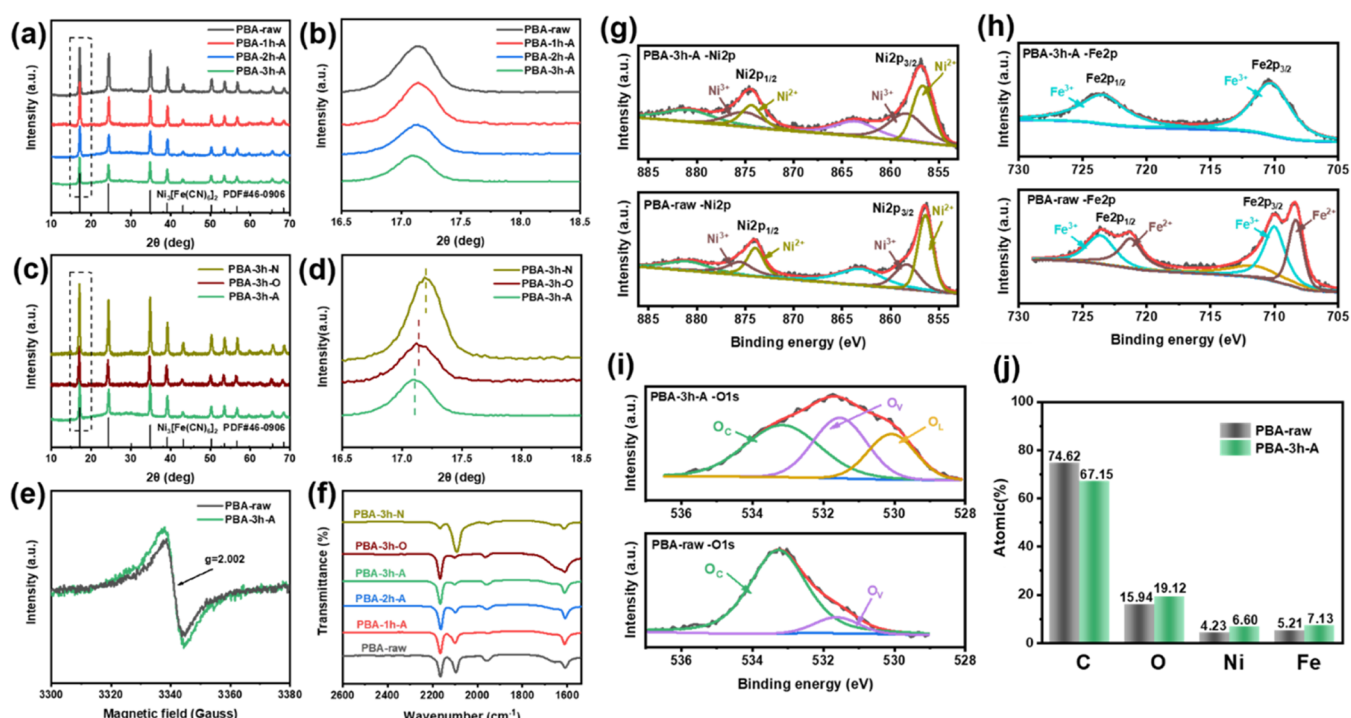


Figure 2. (a) XRD patterns of the PBA under different plasma times. (b) XRD patterns in 16.5–18.5°. (c) XRD patterns of the PBA under different atmospheres. (d) XRD patterns in 16.5–18.5°. (e) Solid electron spin resonance (ESR) spectra of NiFe PBA and PBA-3h-A. (f) Fourier transform infrared (FTIR) spectra. (g–i) High-resolution X-ray photoelectron spectroscopy (XPS) spectra of Ni 2p, Fe 2p, and O 1s of PBA-raw and PBA-3h-A. (j) Corresponding element content by XPS.

C≡N groups without damaging the framework structure. Density functional theory (DFT) results confirm that the induced M–O bonds positively improve the OER activity. After 3 h of DBD air plasma treatment, NiFe PBA electrocatalysts exhibited excellent OER catalytic performance with a low overpotential of 251 mV at 10 mA cm⁻² and 100 h of long-term stability. Driven by a solar silicon chip, the overall electrolysis efficiency of water splitting is up to 64% under real operation conditions.

2. RESULTS AND DISCUSSION

2.1. Material Preparation and Characterization.

Bimetallic cyanide frameworks (NiFe PBAs) were first synthesized by a standing precipitation method (Figure 1a). The obtained solid product is a Ni-based Prussian blue structure with rich defects (Figure S1). The morphology of this pristine NiFe PBA is a standard cubic shape with ~50 nm (Figure 1c,e). For surface modification, as shown in Figure 1b, the synthetic powders were then placed in a DBD device. After a 3 h DBD treatment in the air, the cubic nanostructure broke into smaller squares (Figure 1d), which were concave and rough. A closer inspection of Figure 1f reveals that the edge can be etched for nearly 6 nm, forming an arc edge. The ionized radical groups in air plasma can etch and destroy the unstable amorphous species of NiFe PBA, which is the main cause of morphological changes. Element mapping images show that the DBD treatment only etched the surface without damaging the overall PBA frame structure. Due to the reduction of particles, the specific surface area increases from 55.28 to 83.58 m² g⁻¹ (Figure S2). The pore-size distribution shows that NiFe PBA treated by DBD maintains a high degree of porosity. To detect the details of changes in the core, a closer inspection with high-resolution transmission electron microscopy (HRTEM, Figure 1g) images reveals that atoms are arranged in short-range order and long-range disorder. In the short crystal, a clear crystal lattice fringe spacing of 0.295 and 0.256 nm corresponding to the (222) and (400) plane of NiFe PBA [cubic F43m (216)] can be found. Interestingly, generous crystal defects including edges and amorphous regions labeled by white dash lines also occur in the core, arising from dislocation and distortion by the replacement of Ni/Fe atoms during co-precipitation and plasma process.

Phase structures are identified by an X-ray powder diffractometer (XRD) (Figure 2a). Pristine PBA exhibits a cubic F43m (216) crystal form of Ni₃[Fe(CN)₆]₂ (PDF No. 46-0906). With the extension of the DBD etching time, the crystal peaks change slightly. To compare these data distinctly, the main peak at 17.325° is enlarged in Figure 2b. Owing to the vacancies and distortions observed in the crystal structure (Figure 1g), the intensity of the main peak decreases gradually. The amorphous region accounts for a large proportion. To distinguish the various effect of N₂, O₂, and air, Figure 2c shows the XRD patterns of PBA under various atmospheres. The crystallite peak at 17.325° shifts to the low-angle direction after O₂ and air DBD compared with N₂ (Figure 2d). Table S1 displays that the lattice constants of PBA-3h-A and PBA-3h-O increase compared with that of pristine PBA. Few change of the lattice constants of PBA-3h-N was found. The clear comparison results prove that the lattice distortion is caused by active oxygen rather than N₂. To further understand the reactive species in plasma, optical emission spectroscopy (OES) was performed *in situ* (Figure S3). The highest emission lines in the discharge medium of the plasma jet are

related to atomic oxygen [OI, 3p₂ → 3s₂, (777.42 nm) and 3p₂ → 3s₁, (844.64 nm)], which means that a large number of active oxygen atoms and excited oxygen molecules exist in the plasma state.^{32,33} OES further confirms that just the active oxygen species etch the surface of PBA, causing the lattice distortion of crystal cells. However, how to explain this lattice distortion phenomenon, oxygen vacancies, breaking of C≡N bonds, or doped oxygen atoms?

To detect the oxygen vacancies, electron spin resonance (ESR) spectroscopy was utilized (Figure 2e). ESR signals at *g* = 2.002 correspond to the unpaired electrons trapped by the oxygen vacancies.³⁴ We define the area under the *g* = 2.002 peak as a semiquantitative measure of O_V concentration. A much stronger signal is observed for PBA-3h-A after DBD etching.³⁵ The as-observed enhanced ESR signal can be attributed to the significant increase in oxygen vacancies. Vacancies can dramatically promote the generation and exposure of metal active sites in a catalyst.^{35–38} Therefore, these rich vacancies may dramatically increase the amount of accessible Fe/Ni sites for the electrochemical generation of active NiFeOOH and further improve the OER precatalytic activity of PBA.

Fourier transform infrared (FTIR) spectroscopy further exhibits the changes in functional groups (Figure 2f). The FTIR spectra of precursor PBA confirm the Prussian blue structure. The most intense band corresponds to the principal vibration frequency (ν_{CN}) of the C≡N bridge, associated with the electron transfer from the metal center to the antibonding π^* orbital of the cyanide group.^{39,40} The higher ν_{CN} represents the higher oxidation state of metal cations.^{41–43} In all samples, the presence of an asymmetric band at 2166 cm⁻¹ is attributed to the cyanide vibration in Fe^{III}–C≡N–Ni^{II} configuration, and the 2100 cm⁻¹ band corresponds to the vibration of C≡N in Fe^{II}–C≡N–Ni^{II}.^{41,43–45} Compared to raw Ni₃[Fe(CN)₆]₂, the peak intensity of PBA-A at 2100 cm⁻¹ decreases, while that at 2166 cm⁻¹ increases with the prolonging of the DBD treatment time, indicating a gradual transformation from the Fe^{II}–C≡N–Ni^{II} phase to the Fe^{III}–C≡N–Ni^{II} phase. Vibration peaks of samples treated in O₂ are similar to that in the air but different from that in N₂. Therefore, the substantial increase of Fe oxidation states can be explained by oxygen bonding to the Fe sites as a natural consequence of the interaction with the active oxygen species generated by the plasma. Due to oxidation, the hydrophilicity also changes significantly. Compared with the raw PBA, water droplets spread rapidly on the surface of PBA-3h-A, indicating its superhydrophilic nature (Figure S4). The excellent wettability of PBA-3h-A is conducive to the penetration and adsorption of an electrolyte on the electrode surface.

X-ray photoelectron spectroscopy (XPS) was further conducted to characterize the variational chemical states of Fe and Ni (Figure S5). As seen in Figure 2g, the influence of the DBD plasma on Ni peaks is very small, while a great change in the Fe peaks can be seen in Figure 2h. Compared with the Fe 2p spectrum of PBA-raw, the peaks (708.34 and 721.34 eV) belonging to Fe^{II}(CN)₆ disappear in the Fe 2p spectrum of PBA-3h-A, while two dominant peaks at 710.06 and 723.65 eV attributed to Fe^{III}(CN)₆ become stronger.⁴⁶ This phenomenon implies the presence of intrinsic charge transfer in Fe atoms after DBD plasma. Fe^{III} centers with a more positive charge will facilitate the electrostatic attraction of more anionic intermediates for a fast redox process in the alkaline medium. Figure 2j shows the changes in C and O

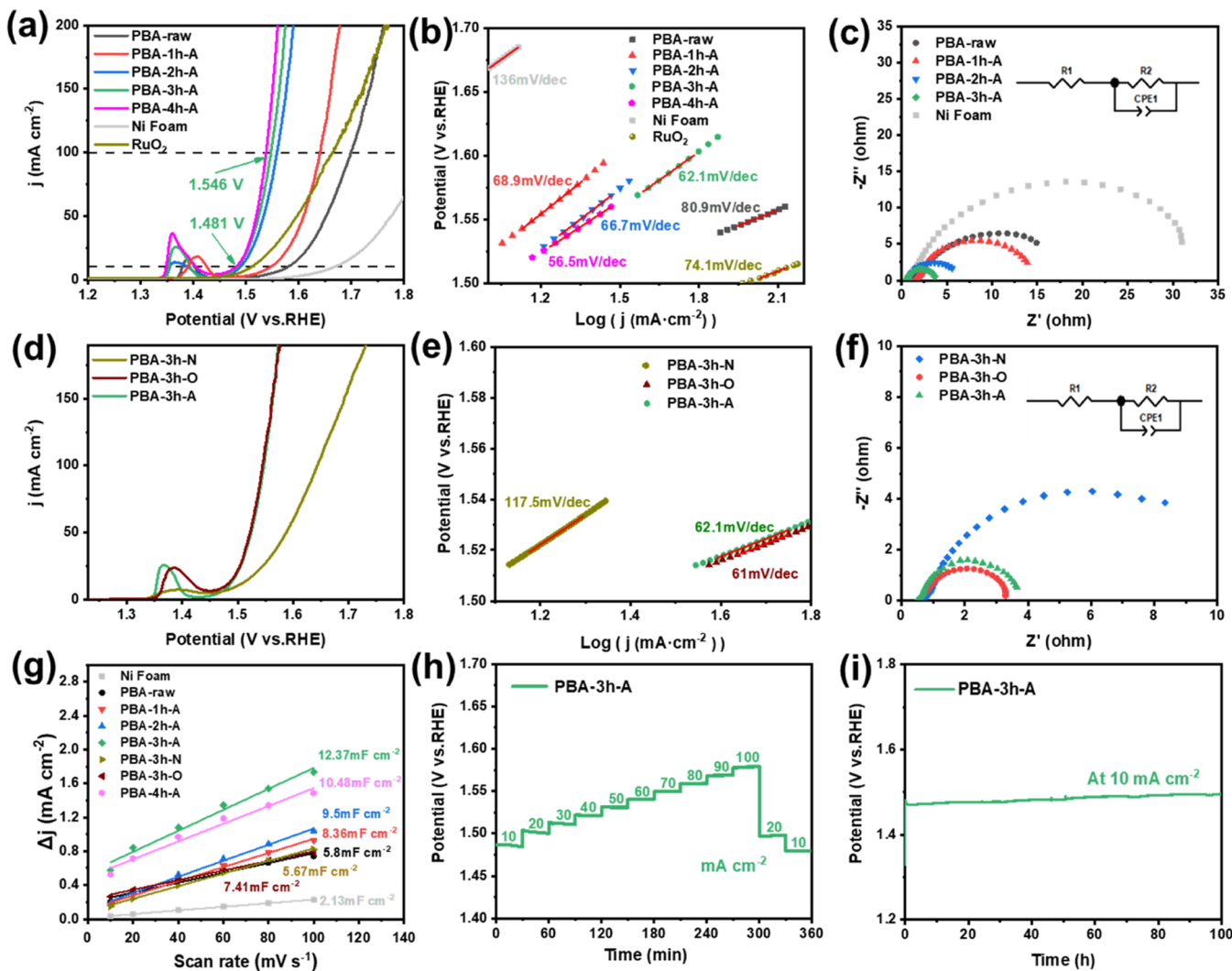


Figure 3. Oxygen evolution reaction electrocatalysis in 1.0 M KOH. (a, d) Polarization curves (1 mV s⁻¹), (b, e) Tafel slopes, (c, f) electrochemical impedance spectra of Ni foam, RuO₂, PBA-raw, PBA-3h-A ($T = 1\text{--}4$ h), PBA-3h-O, and PBA-3h-N. (g) Δj and relative electrochemically active surface area in 1.0 M KOH. (h) Multicurrent process of PBA-3h-A from 10 to 100 and back to 10 mA cm⁻². (i) Chronopotentiometric curves of PBA-3h-A at constant current densities of 10 mA cm⁻². The stability test is without IR compensation. For clarity, the multicurrent step (MCS) results have been divided into two ranges (h) and (i).

content. The increased O element originates from the oxidation of the suspended bonds in ligands by air plasma and the adsorption of O species (O_2 and H_2O) adsorption onto the Fe active site.⁴⁷ Three main peaks in Figure 2i (O_L —lattice oxygen, O_C —adsorbed oxygen, O_V —vacancy oxygen) clearly prove this phenomenon.⁴⁸ Inferring from the appearance of O_L and changes in the C content, the active atomic oxygen under DBD plasma can break part of $C\equiv N$ groups and bond to Fe sites directly. The peak of O_V (percentage increase from 15 to 44%) is assigned to the oxygen-deficient regions within the lattice, which demonstrates the fruitful introduction of oxygen vacancies during the plasma procedure.

2.2. OER Performance. The electrocatalytic OER performance was investigated in a 1.0 M KOH electrolyte by using a standard three-electrode system. In addition, PBA-raw, Ni foam, and RuO₂ were also evaluated at the same criteria for comparison.

In Figure 3a, the pristine PBA exhibits a large overpotential of 349 mV at the current density of 10 mA cm⁻² (η_{10}), which

is consistent with the previous report.^{24,29,49} After the plasma treatment for 1, 2, and 3 h, η_{10} is significantly reduced to 317, 260, and 251 mV, respectively. Even at 100 mA cm⁻², the PBA-3h-A sample still shows a very low overpotential of only 316 mV. In Figure 3b, the PBA-3h-A catalyst displays a lower Tafel slope of 62.1 mV dec⁻¹ compared to RuO₂/NF (74.1 mV dec⁻¹). The DBD treatment effectively improves the OER activity in terms of the overpotential and Tafel slope; however, this improvement gradually decreases after 3 h. The charge-transfer resistance (R_{ct} , Figure 3) reveals that the enhanced charge-transfer kinetics benefited from DBD treatment time. We also explored the influence of N_2 , O_2 , and air on the catalytic performance of PBA (Figure 3d). The linear sweep voltammetry (LSV) curves and Tafel slopes obtained in O_2 and air are mostly similar, while on the contrary in N_2 , very poor performance (Figure 3e). Charge-transfer resistance indicates the enhanced kinetics in the PBA-3h-A and PBA-3h-O electrodes (Figure 3f). The cyclic voltammetry (CV) curves with different scan rates are shown in Figure S6. The corresponding electrochemical double-layer capacitance value

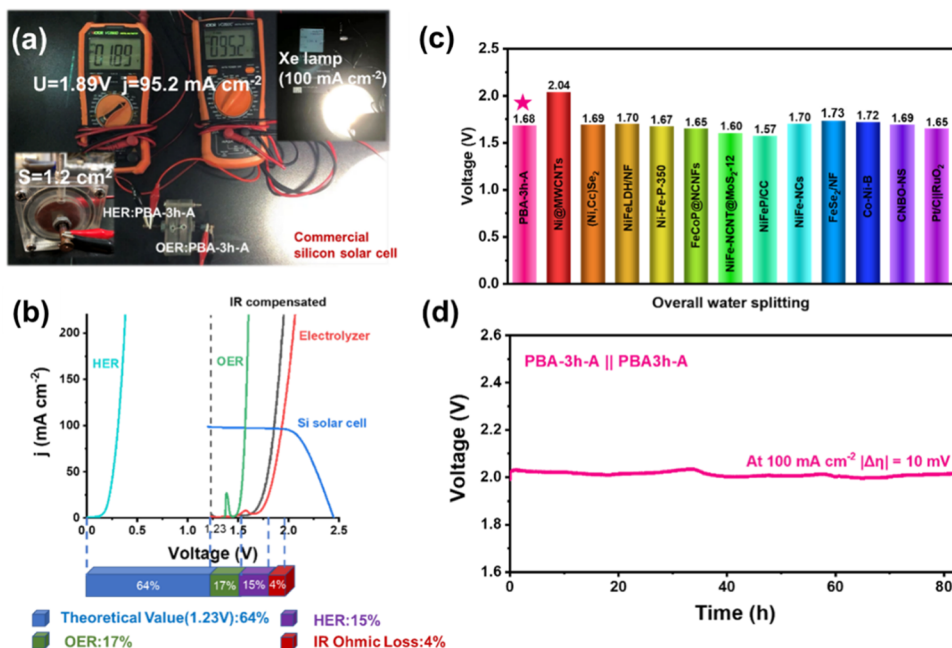


Figure 4. (a) Photographs of the electrolyzer powered by a commercial polycrystalline Si solar cell under AM 1.5 conditions (100 mW cm^{-2}). (b) Polarization curves of the two electrodes and the electrolyzer (with and without IR compensation, 1 mV s^{-1}) with PBA-3h-A as both cathode and anode, giving the energy utilization of the electrolysis cell. (c) Comparison of η_{10} for this work and other OER literature. (d) Cell voltage during galvanostatic electrolysis at 100 mA cm^{-2} . The stability test is without IR compensation.

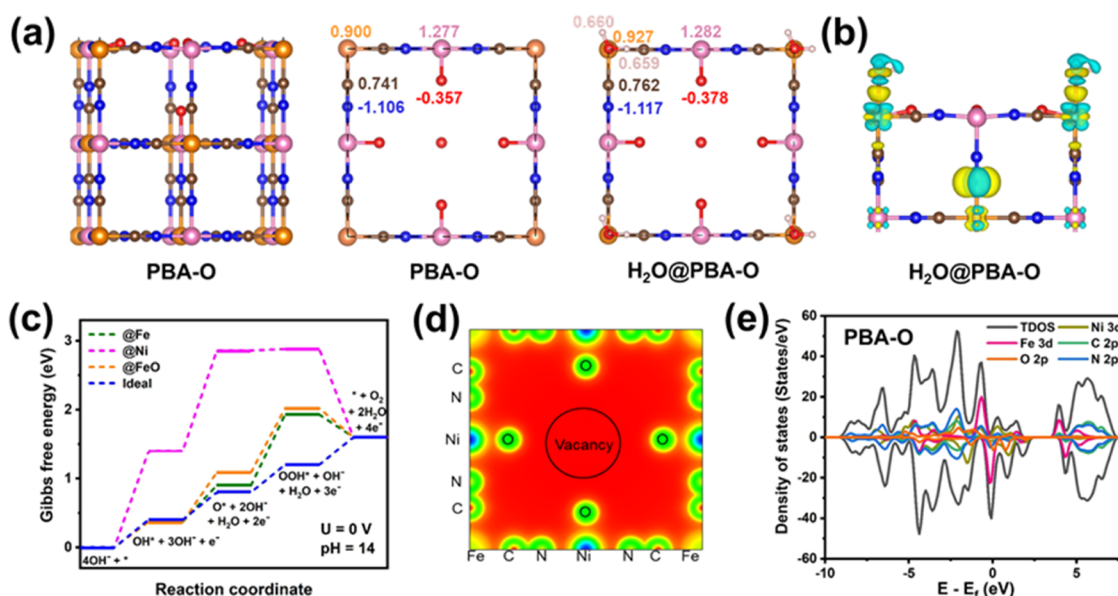


Figure 5. (a) Side and top view geometrical structures of PBA-O and relative Bader charges of PBA-O and $\text{H}_2\text{O}@$ PBA-O. (b) Charge density difference map of $\text{H}_2\text{O}@$ PBA-O. (c) Gibbs free energy profiles of the four-step OER process over Fe, Ni, and FeO sites at $U = 0 \text{ V}$ and $\text{pH} = 14$ (Fe, Ni for PBA and FeO, NiO for PBA-O). (d) Electrostatic potential of PBA-O. The red and blue colors represent the maximum (positive) and minimum (negative) potentials, respectively. (e) Total density of states (TDOS) and partial density of states (PDOS) of PBA-O.

(C_{dl}), in Figure 3g, exhibits that the C_{dl} value of PBA-3h-A (12.37 mF cm^{-2}) is much larger than that of PBA-raw (5.8 mF cm^{-2}), suggesting that more catalytic reaction sites are exposed to the electrolyte after DBD modification. The electrochemical active surface area (ECSA) values and the corresponding normalized polarization curves are shown in Figures S7 and S8. DBD plasma significantly improves the intrinsic activity of the catalysts toward OER.

The electrochemical stability of the PBA-3h-A electrode was evaluated by multicurrent steps (MCS, Figure 3h,i). First, with

the increasing current density, the overpotential increases step by step. When the current density is switched back to 10 mA cm^{-2} , the overpotential retains at 252 mV stably. After a continuous 100 h long-term test, the overpotential increases by not more than 20 mV . The SEM images in Figure S9 show that the PBA particles still attach to the fibers of Ni foam uniformly and some nanosheets occur after OER testing. The insight into the OER process is provided by a Raman spectrometer (Figure S10a). During the activation process, NiFeOOH can be generated from NiFe PBA after 20 CV cycles since Raman

shifts appear at 473 and 550 cm^{-1} , which can be related to the E_g bending vibration and A_{1g} stretching vibration in NiFeOOH active species.^{5,25} Meanwhile, the XRD (Figure S10b) diffraction peaks of NiFe PBA disappear and no other new peaks occur, indicating that the PBA crystal gradually transforms into amorphous NiFeOOH during the OER process.⁵¹

Compared with other traditional modification methods (high-temperature plasma, calcination, hydrothermal) in Table S2, the room-temperature DBD process preserves the PBA framework structure to the maximum extent and achieves charge redistribution *in situ*. The retention of high dispersion of metal active sites promotes PBA-3h-A with low water splitting potential and ultrapersistent stability. In this work, DBD plasma exhibits convenience, high chemical reactivity, and low thermal effect, making it an effective room-temperature *in situ* etching method.

2.3. Overall Splitting Performance. The PBA-3h-A electrode was then evaluated as both cathode and anode in a solar cell-driven alkaline electrolyzer produce H_2 and O_2 using solar energy (Figure 4a). At sun radiation of 100 mW cm^{-2} , the current density of the OERa||HER system can reach 95.2 mA cm^{-2} at the working voltage of only 1.89 V (Figure 4a). Because of the relatively poor HER catalytic activity (Figure S11), the efficiency loss of HER is 15%. The overall electrolysis efficiency is ~64% under the real operation conditions (Figure 4b). If the cathode is replaced with Pt/C, a higher energy efficiency can be obtained.

Compared with the overall water splitting of other Ni/Fe-based bifunctional catalysts (Figure 4c and Table S3), 1.68 V of PBA-3h-A is superior to most catalysts at 10 mA cm^{-2} .^{50,52,53} At 100 mA cm^{-2} current densities, the overpotential of the OERa||HER system is just 1.99 V and can be maintained for over 80 h (Figure 4d). The long-time continuous test highlights superior durability. This PBA-3h-A catalyst features a low splitting potential at a high current density, which is attributed to the highly dispersed active sites obtained by the DBD plasma. The excellent catalytic performance endows the NiFe PBA with practical value in H_2 generation from water splitting.

2.4. DFT Calculations. The DFT theory was further applied to calculate the electronic properties and OER mechanism of PBA and PBA-O to reveal the intrinsic reasons for the better OER activity of PBA-O. In Figures 5a and S12a, the Bader charges of surface ions indicate that the valence electrons of Ni, N, and C tend to shift to surface O due to the charge redistribution after O_2 plasma. Compared to the pristine PBA, PBA-O is more propitious to adsorb H_2O , which is the entrance channel of the OER process. H_2O favors adsorbing at the top of the Fe site in PBA and FeO site in PBA-O, while the latter occurs with a lower adsorption energy of -0.52 eV, which is 0.46 eV lower than that in pristine PBA. After adsorption, ~0.126 electrons shift from the H_2O group to PBA-O, while only 0.110 electrons shift in the pristine PBA (Figures 5b and S12b). The bond lengths of Fe-OH₂ and Fe-OH₂ are relatively 2.120 and 2.106 Å, respectively, which also elucidates the enhanced interaction between PBA-O and H_2O .

The adsorption properties of O^* , OH^* , and OOH^* were carefully examined with the structures depicted in Figure S13. Gibbs free energies (ΔG_{ads}) in PBA-O are slightly higher than that in pristine PBA, implying that the $\text{Fe}(\text{CN})_6$ deficiency and oxygen-rich conditions weaken the association between the adsorbates and FeO/NiO sites.

To comply with the experimental condition, the ΔG_{ads} profiles of the OER mechanism were performed under pH = 14 and U = 0 V (Table S5 and Figure 5c). Over the Fe site, the formation of OOH^* is the rate-determining step (RDS) with $\Delta_t G$ of 1.03 eV. The overpotential η_{OER} is therefore 0.63 V. For the Ni site, the deprotonation of OH^* is the RDS with η_{OER} of 1.06 V. The total and partial density of states of PBA (Figure S14) also suggest that the Fe site is more active than the Ni site around the Fermi level. Hence, the OER efficiency of pristine PBA is determined by the reactions over Fe sites. Similarly, the electrochemical efficiency of PBA-O is also determined by the FeO site. The RDS over the FeO site is the formation of OOH^* with the overpotential η_{OER} of 0.53 V, which is 0.10 V lower than that in pristine PBA. The OER over the oxygen-rich NiO site is difficult as the first step ($\Delta_t G = 1.92$ eV) occurs with a high overpotential η_{OER} of 1.52 V. Figure 5d illustrates that NiO sites are more negative than FeO sites. The partial density of states (Figure 5e) also confirms the essential role of the FeO site in reacting with oxygen species since Fe 3d orbitals dominate the density of states around the Fermi level. The above results suggest that FeO sites can offer more proper interaction with the adsorbates than Fe sites.

To sum, DFT calculations prove that introducing $\text{Fe}(\text{CN})_6$ vacancy and extra oxygen atoms leads to charge redistribution and charge deficiency of the system and finally delivers good OER performance to PBA-O via increasing the adsorption activity to H_2O and reducing the overpotential by 0.10 V. Additionally, the overpotentials η_{OER} is determined by the thermodynamic feasibility of OOH^* formation, which is strongly correlated with the values of $\Delta G_{\text{ads}}(\text{OOH}^*) - \Delta G_{\text{ads}}(\text{O}^*)$.

3. CONCLUSIONS

Herein, the DBD plasma strategy can excite reactive oxygen in the air to etch the $\text{Fe}(\text{CN})_6$ group portion of the PBA framework at room temperature. Importantly, this DBD treatment not only preserves the structural integrity of the porous nanoframework but also establishes Fe sites bound to oxygen *in situ*, thereby tuning the local electronic structure and coordination environment. DFT calculations indicate that the four-electron OER favors proceeding over FeO sites and the RDS is attributed to the formation of OOH^* , which is affected by the difference in adsorption Gibbs free energies of OOH^* and O^* . The DBD treatment leads to charge distribution of surface ions, and Fe sites after modification can offer proper interaction with the adsorbates, thus improving the OER performance by narrowing the overpotential of 0.1 V. The excellent OER performance is featured for an overpotential of only 251 mV at 10 mA cm^{-2} and 316 mV at 100 mA cm^{-2} current density. In an HER||OER electrolysis cell, only by NiFe PBA, the voltage is 1.99 V at 100 mA cm^{-2} , operating continuously for more than 80 h. The DBD plasma provides a flexible and safe route for the development of high-performance catalysts from a nondestructive modification of widely available framework structures.

■ ASSOCIATED CONTENT

SI Supporting Information

The Supporting Information is available free of charge at <https://pubs.acs.org/doi/10.1021/acs.inorgchem.3c00999>.

Additional details on the experimental materials and methods; EDX spectrum; pore-size distribution curves;

optical emission spectroscopy; water contact angle; XPS full spectrum; CV curves for C_{dl} ; ex situ XRD, Raman, and SEM images; theoretical calculation model; and tables for cell parameters, performance comparison, and Gibbs free energy ([PDF](#))

AUTHOR INFORMATION

Corresponding Authors

Guo-Ling Li — Institute of Materials for Energy and Environment, College of Materials Science and Engineering, Qingdao University, Qingdao 266071, China;  [orcid.org/0000-0002-1320-2045](#); Email: liguoling@qdu.edu.cn

Hai-Jie Cao — Institute of Materials for Energy and Environment, College of Materials Science and Engineering, Qingdao University, Qingdao 266071, China; Email: caohj@qdu.edu.cn

Author

Wen-Bin Wang — Institute of Materials for Energy and Environment, College of Materials Science and Engineering, Qingdao University, Qingdao 266071, China

Complete contact information is available at:

<https://pubs.acs.org/10.1021/acs.inorgchem.3c00999>

Author Contributions

G.-L.L. conceived the idea and designed the experiment. W.-B.W. carried out the sample synthesis, characterization, and electrochemical measurement. H.-J.C. carried out the theoretical calculations. The manuscript was written through contributions of all authors.

Notes

The authors declare no competing financial interest.

ACKNOWLEDGMENTS

The authors acknowledge the National Natural Science Foundation of China (No. 51804174).

REFERENCES

- (1) Yu, Z. Y.; Duan, Y.; Feng, X. Y.; Yu, X. X.; Gao, M. R.; Yu, S. H. Clean and Affordable Hydrogen Fuel from Alkaline Water Splitting: Past, Recent Progress, and Future Prospects. *Adv. Mater.* **2021**, *33*, No. 2007100.
- (2) Li, S. S.; Gao, Y. Q.; Li, N.; Ge, L.; Bu, X. H.; Feng, P. Y. Transition metal-based bimetallic MOFs and MOF-derived catalysts for electrochemical oxygen evolution reaction. *Energy Environ. Sci.* **2021**, *14*, 1897–1927.
- (3) Ding, K. X.; Hu, J. G.; Jin, W.; Zhao, L. M.; Liu, Y. P.; Wu, Z. H.; Weng, B. C.; Hou, H. S.; Ji, X. B. Diamion Induced Electron Delocalization of Trifunctional Electrocatalysts for Rechargeable Zn-Air Batteries and Self-Powered Water Splitting. *Adv. Funct. Mater.* **2022**, *32*, No. 2201944.
- (4) Chen, H.; Huang, H. B.; Li, H. H.; Zhao, S. Z.; Wang, L. D.; Zhang, J.; Zhong, S. L.; Lao, C. F.; Cao, L. M.; He, C. T. Self-Supporting Co/CeO₂ Heterostructures for Ampere-Level Current Density Alkaline Water Electrolysis. *Inorg. Chem.* **2023**, *62*, 3297–3304.
- (5) Kong, X. L.; Zhao, X. H.; Li, C.; Jia, Z. M.; Yang, C. K.; Wu, Z. Y.; Zhao, X. D.; Zhao, Y.; He, F.; Ren, Y. M.; Yang, P. P.; Liu, Z. L. Terminal Group-Oriented Self-Assembly to Controllably Synthesize a Layer-by-Layer SnSe₂ and MXene Heterostructure for Ultrastable Lithium Storage. *Small* **2023**, *19*, No. 2206563.
- (6) Meena, A.; Thangavel, P.; Nissimagoudar, A. S.; Singh, A. N.; Jana, A.; Jeong, D.; Im, H.; Kim, K. S. Bifunctional oxovanadate doped cobalt carbonate for high-efficient overall water splitting in alkaline-anion-exchange-membrane water-electrolyzer. *Chem. Eng. J.* **2022**, *430*, No. 132623.
- (7) Harzandi, A. M.; Shadman, S.; Nissimagoudar, A. S.; Kim, D. Y.; Lim, H. D.; Lee, J. H.; Kim, M. G.; Jeong, H. Y.; Kim, Y.; Kim, K. S. Ruthenium Core–Shell Engineering with Nickel Single Atoms for Selective Oxygen Evolution via Nondestructive Mechanism. *Adv. Energy Mater.* **2021**, *11*, No. 2003448.
- (8) Sun, X. P.; Zhang, Y. H.; Xiao, Y.; Li, Z. Q.; Wei, L. Z.; Yao, G.; Niu, H. L.; Zheng, F. C. Surface Reconstruction of Co₄N Coupled with CeO₂ toward Enhanced Alkaline Oxygen Evolution Reaction. *Inorg. Chem.* **2022**, *61*, 14140–14147.
- (9) Liu, X.; Zhang, J. F.; Zheng, C. Y.; Xue, J. D.; Huang, T.; Yin, Y.; Qin, Y. Z.; Jiao, K.; Du, Q.; Guiver, M. D. Oriented proton-conductive nano-sponge-facilitated polymer electrolyte membranes. *Energy Environ. Sci.* **2020**, *13*, 297–309.
- (10) Lai, C. L.; Li, H. M.; Sheng, Y.; Zhou, M.; Wang, W.; Gong, M. X.; Wang, K. L.; Jiang, K. 3D Spatial Combination of CN Vacancy-Mediated NiFe-PBA with N-Doped Carbon Nanofibers Network Toward Free-Standing Bifunctional Electrode for Zn–Air Batteries. *Adv. Sci.* **2022**, *9*, No. 2105925.
- (11) Qiao, Y.; Jiang, K.; Deng, H.; Zhou, H. A High-Energy-Density and Long-Life Lithium-Ion Battery via Reversible Oxide–Peroxide conversion. *Nat. Catal.* **2019**, *2*, 1035–1044.
- (12) Ananthraj, S.; Kundu, S.; Noda, S. "The Fe Effect": A review unveiling the critical roles of Fe in enhancing OER activity of Ni and Co based catalysts. *Nano Energy* **2021**, *80*, No. 105514.
- (13) Xuan, C.; Wang, J.; Xia, W.; Zhu, J.; Peng, Z.; Xia, K.; Xiao, W.; Xin, H. L.; Wang, D. Heteroatom (P, B, or S) incorporated NiFe-based nanocubes as efficient electrocatalysts for the oxygen evolution reaction. *J. Mater. Chem. A* **2018**, *6*, 7062–7069.
- (14) Zhang, B.; Wu, Z. H.; Shao, W. J.; Gao, Y.; Wang, W. W.; Ma, T.; Ma, L.; Li, S.; Cheng, C.; Zhao, C. S. Interfacial Atom-Substitution Engineered Transition-Metal Hydroxide Nanofibers with High-V alence Fe for Efficient Electrochemical Water Oxidation. *Angew. Chem., Int. Ed.* **2022**, *61*, No. e202115331.
- (15) Sun, H. C.; Tung, C. W.; Qiu, Y.; Zhang, W.; Wang, Q.; Li, Z. S.; Tang, J.; Chen, H. C.; Wang, H. C.; Chen, H. M. Atomic Metal–Support Interaction Enables Reconstruction-Free Dual-Site Electrocatalyst. *J. Am. Chem. Soc.* **2022**, *144*, 1174–1186.
- (16) Qiao, X. S.; Kang, H. J.; Li, Y.; Cui, K.; Jia, X.; Wu, X. H.; Qin, W. Novel FeNi-Based Nanowires Network Catalyst Involving Hydrophilic Channel for Oxygen Evolution Reaction. *Small* **2022**, *18*, No. 2106378.
- (17) Luo, W. H.; Wang, Y.; Luo, L. X.; Gong, S.; Wei, M. N.; Li, Y. X.; Gan, X. P.; Zhao, Y. Y.; Zhu, Z. H.; Li, Z. Single-Atom and Bimetallic Nanoalloy Supported on Nanotubes as a Bifunctional Electrocatalyst for Ultrahigh-Current-Density Overall Water Splitting. *ACS Catal.* **2022**, *12*, 1167–1179.
- (18) Zhao, M.; Yuan, K.; Wang, Y.; Li, G.; Guo, J.; Gu, L.; Hu, W.; Zhao, H.; Tang, Z. Metal-organic frameworks as selectivity regulators for hydrogenation reactions. *Nature* **2016**, *539*, 76–80.
- (19) Mu, X. Q.; Yuan, H. M.; Jing, H. Y.; Xia, F. J.; Wu, J. S.; Gu, X. Y.; Chen, C. Y.; Bao, J. C.; Liu, S. L.; Mu, S. C. Superior electrochemical water oxidation in vacancy defect-rich 1.5 nm ultrathin trimetal-organic framework nanosheets. *Appl. Catal., B* **2021**, *296*, No. 120095.
- (20) Li, H.; Li, L.; Lin, R.-B.; Zhou, W.; Zhang, Z.; Xiang, S.; Chen, B. Porous metal-organic frameworks for gas storage and separation: status and challenges. *Energy Chem.* **2019**, *1*, No. 100006.
- (21) Cao, L. M.; Lu, D.; Zhong, D. C.; Lu, T. B. Prussian blue analogues and their derived nanomaterials for electrocatalytic water splitting. *Coord. Chem. Rev.* **2020**, *407*, No. 213156.
- (22) Thangavel, P.; Ha, M. R.; Kumaraguru, S.; Meena, A.; Singh, A. N.; Harzandi, A. M.; Kim, K. S. Graphene-nanoplatelets-supported NiFe-MOF: high-efficiency and ultra-stable oxygen electrodes for sustained alkaline anion exchange membrane water electrolysis. *Energy Environ. Sci.* **2020**, *13*, 3447–3458.
- (23) Meena, A.; Thangavel, P.; Jeong, D.; Singh, A. N.; Jana, A.; Im, H.; Nguyen, D. A.; Kim, K. S. Crystalline-amorphous interface of

- mesoporous Ni₂P @ FePO_xH_y for oxygen evolution at high current density in alkaline-anion-exchange-membrane water-electrolyzer. *Appl. Catal., B* 2022, 306, No. 121127.
- (24) Zhang, G. X.; Li, Y. L.; Xiao, X.; Shan, Y.; Bai, Y.; Xue, H. G.; Pang, H.; Tian, Z. Q.; Xu, Q. In Situ Anchoring Polymetallic Phosphide Nanoparticles within Porous Prussian Blue Analogue Nanocages for Boosting Oxygen Evolution Catalysis. *Nano Lett.* 2021, 21, 3016–3025.
- (25) Yilmaz, G.; Tan, C. F.; Hong, M.; Ho, G. W. Functional Defective Metal-Organic Coordinated Network of Mesostructured Nanoframes for Enhanced Electrocatalysis. *Adv. Funct. Mater.* 2018, 28, No. 1704177.
- (26) Bennett, T. D.; Cheetham, A. K.; Fuchs, A. H.; Coudert, F.-X. Interplay between defects, disorder and flexibility in metal-organic frameworks. *Nat. Chem.* 2017, 9, 11.
- (27) Xu, S.; Niu, M.; Zhao, G. W.; Ming, S. J.; Li, X. Y.; Zhu, Q. L.; Ding, L. X.; Kim, M. J.; Alothman, A. A.; Mushab, M. S. S.; Yamauchi, Y. Size control and electronic manipulation of Ru catalyst over B, N codoped carbon network for high-performance hydrogen evolution reaction. *Nano Res.* 2023, 16, 6212–6219.
- (28) Zhang, W.; Song, H.; Cheng, Y.; Liu, C.; Wang, C.; Khan, M. A. N.; Zhang, H.; Liu, J.; Yu, C.; Wang, L. Core–Shell Prussian Blue Analogs with Compositional Heterogeneity and Open Cages for Oxygen Evolution Reaction. *Adv. Sci.* 2019, 6, No. 1801901.
- (29) Yu, Z. Y.; Duan, Y.; Liu, J. D.; Chen, Y.; Liu, X. K.; Liu, W.; Ma, T.; Li, Y.; Zheng, X. S.; Yao, T.; Gao, M. R.; Zhu, J. F.; Ye, B. J.; Yu, S. H. Unconventional CN vacancies suppress iron-leaching in Prussian blue analogue pre-catalyst for boosted oxygen evolution catalysis. *Nat. Commun.* 2019, 10, No. 2799.
- (30) Kang, Y.; Wang, S.; Hui, K. S.; Li, H. F.; Liang, F.; Wu, X. L.; Zhang, Q.; Zhou, W.; Chen, L.; Chen, F.; Hui, K. N. Fe(CN)₆ vacancy-boosting oxygen evolution activity of Co-based Prussian blue analogues for hybrid sodium-air battery. *Mater. Today Energy* 2021, 20, No. 100572.
- (31) Neyts, E. C.; Ostrikov, K. K.; Sunkara, M. K.; Bogaerts, A. Plasma Catalysis: Synergistic Effects at the Nanoscale. *Chem. Rev.* 2015, 115, 13408.
- (32) Falahat, A.; Ganjavi, A.; Taraz, M.; Ravari, M. N. R.; Shahedi, A. Optical characteristics of a RF DBD plasma jet in various Ar/O₂ mixtures. *Pramana* 2018, 90, No. 27.
- (33) Yehia, S. A.; Petrea, N.; Grigoriu, N.; Vizireanu, S.; Zarif, M. E.; Carpen, L. G.; Ginghina, R. E.; Dinescu, G. Organophosphorus toxic compounds degradation in aqueous solutions using single filament dielectric barrier discharge plasma jet source. *J. Water Process. Eng.* 2022, 46, No. 102637.
- (34) Qian, K. C.; Yan, Y.; Xi, S. B.; Wei, T.; Dai, Y. H.; Yan, X. Q.; Kobayashi, H.; Wang, S.; Liu, W.; Li, R. H. Elucidating the Strain-Vacancy-Activity Relationship on Structurally Deformed Co@CoO Nanosheets for Aqueous Phase Reforming of Formaldehyde. *Small* 2021, 17, No. 2102970.
- (35) Yang, M. Q.; Wang, J.; Wu, H.; Ho, G. W. Noble Metal-Free Nanocatalysts with Vacancies for Electrochemical Water Splitting. *Small* 2018, 14, No. 1703323.
- (36) Zhang, L.; Lu, C. J.; Ye, F.; Wu, Z. Y.; Wang, Y. A.; Jiang, L.; Zhang, L.; Cheng, C.; Sun, Z. M.; Hu, L. F. Vacancies boosting strategy enabling enhanced oxygen evolution activity in a library of novel amorphous selenite electrocatalysts. *Appl. Catal., B* 2021, 284, No. 119758.
- (37) Wygant, B. R.; Kawashima, K.; Mullins, C. B. Catalyst or Precatalyst? The Effect of Oxidation on Transition Metal Carbide, Pnictide, and Chalcogenide Oxygen Evolution Catalysts. *ACS Energy Lett.* 2018, 3, 2956–2966.
- (38) Anantharaj, S.; Sugime, H.; Chen, B.; Akagi, N.; Noda, S. Achieving Increased Electrochemical Accessibility and Lowered Oxygen Evolution Reaction Activation Energy for Co²⁺ Sites with a Simple Anion Preoxidation. *J. Phys. Chem. C* 2020, 124, 9673–9684.
- (39) Zhao, Y. B.; Liang, B. L.; Wei, X. J.; Li, K. X.; Lv, C. C.; Zhao, Y. A core–shell heterostructured CuFe@NiFe Prussian blue analogue as a novel electrode material for high-capacity and stable capacitive deionization. *J. Mater. Chem. A* 2019, 7, 10464.
- (40) Kulesza, P. J.; Malik, M. A.; Denca, A.; Strojek, J. In situ FT-IR/ATR spectroelectrochemistry of Prussian Blue in the solid state. *Anal. Chem.* 1996, 68, 2442–2446.
- (41) Goberna-Ferrón, S.; Hernandez, W. Y.; Rodriguez-García, B.; Galan-Mascaro, J. R. Light-Driven Water Oxidation with Metal Hexacyanometallate Heterogeneous Catalysts. *ACS Catal.* 2014, 4, 1637–1641.
- (42) de Tacconi, N. R.; Rajeshwar, K.; Lezna, R. O. Metal Hexacyanoferrates: Electrosynthesis, in Situ Characterization, and Applications. *Chem. Mater.* 2003, 15, 3046.
- (43) Lezna, R. O.; Romagnoli, R.; de Tacconi, N. R.; Rajeshwar, K. Cobalt Hexacyanoferrate: Compound Stoichiometry, Infrared Spectroelectrochemistry, and Photoinduced Electron Transfer. *J. Phys. Chem. B* 2002, 106, 3612.
- (44) Pajerowski, D. M.; Gardner, J. E.; Talham, D. R.; Meisel, M. W. Anisotropic magnetism in Prussian blue analogue films. *New J. Chem.* 2011, 35, 1320–1326.
- (45) Su, D. W.; McDonagh, A.; Qiao, S. Z.; Wang, G. X. High-Capacity Aqueous Potassium-Ion Batteries for Large-Scale Energy Storage. *Adv. Mater.* 2017, 29, No. 1604007.
- (46) Liu, Z. J.; Wang, Y.; Chen, R.; Chen, C.; Yang, H. T.; Ma, J. M.; Li, Y. F.; Wang, S. Y. Quaternary bimetallic phosphosulphide nanosheets derived from prussian blue analogues: Origin of the ultra-high activity for oxygen evolution. *J. Power Sources* 2018, 403, 90–96.
- (47) Grimaud, A.; Diaz-Morales, O.; Han, B. H.; Hong, W. T.; Lee, Y. L.; Giordano, L.; Stoerzinger, K. A.; Koper, M. T. M.; Shao-Horn, Y. Activating lattice oxygen redox reactions in metal oxides to catalyse oxygen evolution. *Nat. Chem.* 2017, 9, 457–465.
- (48) Zhang, H.; Li, P.; Chen, S. L.; Xie, F.; Riley, D. J. Anodic Transformation of a Core–Shell Prussian Blue Analogue to a Bifunctional Electrocatalyst for Water Splitting. *Adv. Funct. Mater.* 2021, 31, No. 2106835.
- (49) Xu, X. H.; Wang, T.; Su, L.; Zhang, Y. J.; Dong, L. J.; Miao, X. Y. In Situ Synthesis of Superhydrophilic Amorphous NiFe Prussian Blue Analogues for the Oxygen Evolution Reaction at a High Current Density. *ACS Sustainable Chem. Eng.* 2021, 9, 5693–5704.
- (50) Thangavel, P.; Kim, G.; Kim, K. S. Electrochemical integration of amorphous NiFe (oxy) hydroxides on surface-activated carbon fibers for high-efficiency oxygen evolution in alkaline anion exchange membrane water electrolysis. *J. Mater. Chem. A* 2021, 9, 14043.
- (51) Luo, X.; Tan, X.; Ji, P. X.; Ji, P.; Chen, L.; Chen, L.; Yu, J.; Yu, J.; Mu, S. C. Surface reconstruction-derived heterostructures for electrochemical water splitting. *Energy Chem.* 2023, 5, No. 100091.
- (52) Sultan, S.; Ha, M.; Kim, D. Y.; Tiwari, J. N.; Myung, C. W.; Meena, A.; Shin, T. J.; Chae, K. H.; Kim, K. S. Superb water splitting activity of the electrocatalyst Fe₃Co(PO₄)₄ designed with computation aid. *Nat. Commun.* 2019, 10, No. 5195.
- (53) Dang, N. K.; Tiwari, J. N.; Sultan, S.; Meena, A.; Kim, K. S. Multi-site catalyst derived from Cr atoms-substituted CoFe nanoparticles for high-performance oxygen evolution activity. *Chem. Eng. J.* 2021, 404, No. 126513.